CrossMark

ORIGINAL PAPER

Triassic emplacement age of the Kalkfeld complex, NW Namibia: implications for carbonatite magmatism and its relationship to the Tristan Plume

U. Kramm[1] · T. Körner[1] · M. Kittel[2] · H. Baier[3] · S. Sindern[1]

Abstract Rb–Sr whole-rock and mineral isotope data from nepheline syenite, tinguaite, and carbonatite samples of the Kalkfeld Complex within the Damaraland Alkaline Province, NW Namibia, indicate a date of 242 ± 6.5 Ma. This is interpreted as the age of final magmatic crystallization in the complex. The geological position of the complex and the spatially close relationship to the Lower Cretaceous Etaneno Alkaline Complex document a repeated channeling of small-scale alkaline to carbonatite melt fractions along crustal fractures that served as pathways for the mantle-derived melts. This is in line with Triassic extensional tectonic activity described for the nearby Omaruru Lineament–Waterberg Fault system. The emplacement of the Kalkfeld Complex more than 100 Ma prior to the Paraná-Etendeka event and the emplacement of the Early Cretaceous Damaraland intrusive complexes excludes a genetic relationship to the Tristan Plume. The initial εSr–εNd pairs of the Kalkfeld rocks are typical of younger African carbonatites and suggest a melt source, in which EM I and HIMU represent dominant components.

✉ U. Kramm
  kramm@rwth-aachen.de

1 Institut für Angewandte Mineralogie und Lagerstättenlehre, RWTH Aachen University, Aachen, Germany

2 Laboratory of Machine Tools and Production Engineering, RWTH Aachen University, Aachen, Germany

3 Institute for Mineralogy, WWU Münster, Münster, Germany

Introduction

The voluminous Early Cretaceous tholeiite extrusions of the Paraná-Etendeka large igneous province and the subsequent opening of the South Atlantic Ocean have been attributed to the upwelling of the Tristan Plume (e.g., Siedner and Mitchell 1976; White and McKenzie 1989; Thompson and Gibson 1991; Turner et al. 1994; Thompson et al. 2001). Precise dating of the volcanic activity documents a very short phase of extrusions between 135 and 132 Ma (e.g., Hawkesworth et al. 1992; Milner et al. 1995), and Renne et al. (1992) suggest that the complete pile of the Paraná lavas erupted within less than 1 Ma.

Post-Palaeozoic emplacements of major alkaline igneous complexes in the close surroundings of the Paraná-Etendeka Province have been described for the Damaraland Alkaline Province, NW Namibia (e.g. Martin et al. 1960; Harris 1995; Trumbull et al. 2000), for SW Angola (Alberti et al. 1999) and for Eastern Paraguay (Comin-Chiaramonti et al. 2007a). Age data for the complexes of NW Namibia, e.g., for Brandberg (Schmitt et al. 2000), for Erongo (Wigand et al. 2004), for Messum and Okorusu (Milner et al. 1995) suggest an Early Cretaceous emplacement period coinciding with the Paraná-Etendeka volcanism in its initial phase, but extending for 10–15 Ma beyond the termination of the tholeiite extrusions (Milner et al. 1995). In contrast, six periods of emplacement between Middle Triassic and Palaeocene times have been distinguished for the Paraguay alkaline and carbonatite complexes (Comin-Chiaramonti et al. 2007a). For Cretaceous times, they coincide only in part with the short period of Paraná-Etendeka flood basalt extrusions (Comin-Chiaramonti et al. 2007b).

Magmas of the Damaraland complexes have commonly been interpreted to represent products of, or to contain components of, the upwelling Tristan Plume

Springer

(Milner and Le Roex 1996; Le Roex and Lanyon 1998; Trumbull et al. 2000, 2003). The alkaline and carbonatitic rocks have received particular attention in evaluating the plume model because of their depth of melt formation, their timing with respect to the volcanic activity of the tholeiitic flood basalts, and their low crustal contamination potential (e.g., Trumbull et al. 2000, 2003). However, the long-lasting alkaline and carbonatite magmatism of Eastern Paraguay, repeatedly changing between potassic and sodic, as well as the linear arrangement of the complexes in Paraguay, SW Angola, and NW Namibia led Comin-Chiaramonti et al. (2007a, b), favor a geodynamically induced melt formation model. These authors suggest a lithospheric origin of the alkaline melts and state that "any hypothesis of an asthenospheric plume origin (of the alkaline and carbonatite melts) is not compelling other than as a thermal perturbation of a decompressional environment" (Comin-Chiaramonti et al. 2007a, b).

The alkaline syenitic Etaneno Complex and the nearby, alkaline silicate–carbonatite complexes Kalkfeld, Ondurakorume, and Osongombo (Fig. 1a) play a prominent role in evaluating the sources of their melts within the Damaraland Alkaline Province, and their mutual relationships (Trumbull et al. 2000; Bühn and Trumbull 2003). Of essential importance for this evaluation is the timing of emplacement of the four complexes. So far, however, only for Etaneno has a reliable Rb–Sr age of 134 ± 3 Ma on nepheline syenite whole-rock samples been reported (Müller 1996). It confirms a Lower Cretaceous age of emplacement and thus a temporal relationship with the Paraná-Etendeka event. For Kalkfeld, four fractions of chloritized biotite yield Jurassic K–Ar ages ranging between 153.6 and 172.8 Ma (Ziegler 1992). In contrast to this result, the tectonic position of Kalkfeld and the three other complexes in a narrow arrangement to dykes of the Early Cretaceous Henties Bay-Outjo dyke swarm suggest a close temporal relationship between the dyke emplacements and the intrusion of the complexes (Trumbull et al. 2004).

In this study, we present Rb–Sr and Sm–Nd isotope data for 12 nepheline syenite and 11 tinguaite whole-rock samples from the Kalkfeld complex as well as Rb–Sr data for separated minerals from two of the nepheline syenites. The resulting mineral Rb–Sr isochrons as well as the corresponding initial εSr and εNd data of the whole-rock samples shed new light on the sources and relationships of the alkaline and carbonatite rocks in Kalkfeld and its vicinity. The Kalkfeld isotope signatures allow an evaluation of the mantle components involved in alkaline and carbonatite melt formation and evolution.
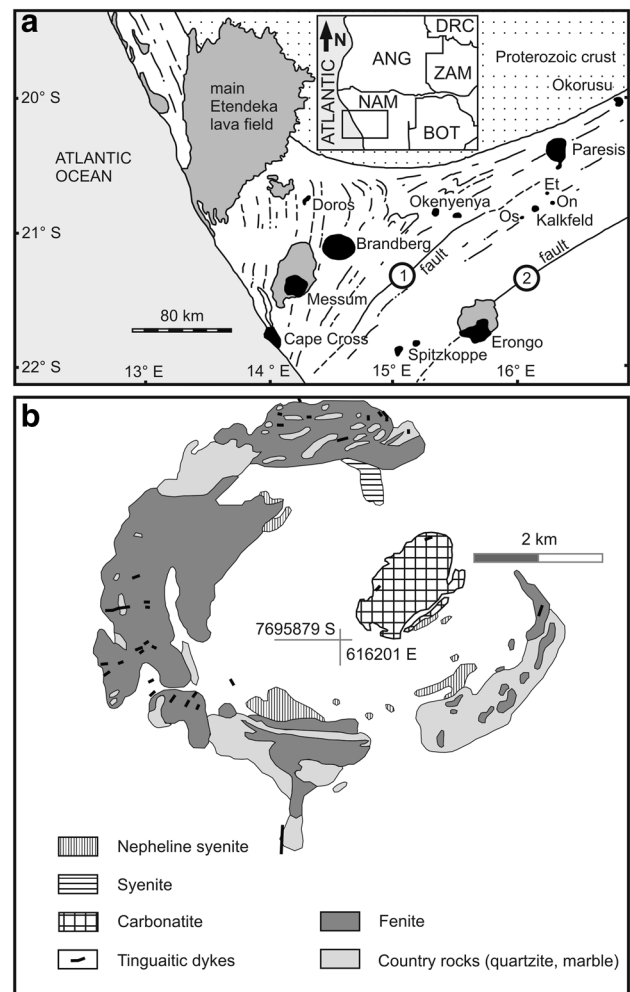
Fig. 1 a Simplified geological sketch map of the study area in NW Namibia: *black*, alkaline and carbonatite complexes (*Et* Etaneno Complex, *On* Ondurakorume Complex, *Os* Osongombo Complex), *grey*, Etendeka lava fields, *black lineations*, faults, and major structures of the Damara orogenic basement with the Autseib Fault–Otjihorongo Thrust *(1)* and the Omaruru Lineament–Waterberg Thrust *(2)*. *Inset* shows the area in southwestern Africa (NAM Namibia, ANG Angola, BOT Botswana, ZAM Zambia, DRC Democratic Republic of Congo), **b** simplified geological map of the Kalkfeld complex after Van Zijl (1962), Verwoerd (1967), Körner (2003)

Geological setting and sampling

The major structural elements of the Neoproterozoic Damara Belt, NW Namibia, reveal a generally northeasterly trending orientation, which was established during the late stages of convergence of the Damara Belt (Miller 1983, 2008, 2013). The alignment of the Mesozoic Damaraland Alkaline Complexes follows this trend (Fig. 1a). Martin et al. (1960), Marsh (1973), Milner et al. (1995), Trumbull et al. (2000, 2003, 2004) and others have suggested, therefore, that the Damara Belt represents a continuing zone of crustal weakness with

a reactivation during the Early Cretaceous break-up of Gondwana. Tectonic reactivation of fault zones during earlier Mesozoic times is reported for the Triassic by Holzförster et al. (1998).

The Kalkfeld Complex and the spatially related Ondurakorume, Etaneno and Osongombo complexes intruded a Late Proterozoic basement of syntectonic granite bodies as well as marbles and schists of the Damara Sequence (Martin et al. 1960; Miller 1983, 2008, 2013). Major shear zones are the Autseib Fault–Otjihorongo Thrust system to the north and the Omaruru Lineament–Waterberg Thrust system towards the south of the four complexes (Fig. 1a). Both lineament structures follow the SW–NE trend. While Kalkfeld, Ondurakorume, and Osongombo likewise are aligned SW–NE, the detailed aeromagnetic and satellite surveys of the Cretaceous Hentjes Bay-Outjo dyke swarm show SSW–NNE running dykes connecting the complexes Kalkfeld and Etaneno (Trumbull et al. 2004).

At the present erosion level, the Kalkfeld Complex represents the subvolcanic part of a central volcano (Le Roex and Lanyon 1998) (Fig. 1b). It shows a classic ring structure with a diameter of about 7 km. A central plug of micaceous sövite and ankeritic sövite (Prins 1981), in major parts metasomatically altered, is surrounded by a belt of poorly exposed nepheline syenite. Fenites, which gradually change from nepheline-bearing into quartz-aegirine-bearing rocks (Körner 2003), separate the alkaline silicate rocks of the central part against the pan-African country rocks (Fig. 1b). A great number of radial and concentric carbonatitic and tinguaitic dykes crosscut carbonatites, nepheline syenites and, importantly, also the fenites, demonstrating late igneous activity. Field evidence for a significant time-gap between the emplacement of the different magmatic rock types is not observed. The structure of the complex, its petrographical and chemical aspects, fluid-induced magma relationships, and the processes of fenitization have been described by Van Zijl (1962); Verwoerd (1966, 1993); Prins (1981); Le Roex and Lanyon (1998); Bühn and Rankin (1999); Trumbull et al. (2000); Bühn et al. (2001); Körner et al. (2001); Bühn and Trumbull (2003); Körner (2003), and Bühn (2008).

Representative nepheline syenite and tinguaite samples investigated for this study were collected from outcrops across the whole area and include dyke rocks from carbonatite, nepheline syenite, and fenite hosts. Petrographic analyses prove these samples to be unweathered. In addition, our set of samples includes two nepheline syenites of Bühn and Trumbull (2003), KF 201 and KF 203, which here are reinvestigated for their isotopic Rb–Sr and Sm–Nd systematics. The geographical positions of the samples within the complex are given as UTM coordinates in Table 1.

Analytical procedures

Major and trace element abundances of powdered whole-rock samples prepared in a tungsten carbide mill were determined by energy dispersive polarized X-ray fluorescence (Spectro XLab2000, Ametek Spectro Analytical Instuments, Kleve, Germany) at RWTH Aachen University. For major element analysis, the samples were dried at $110\,°C$ prior to determination of loss on ignition by heating the sample for 120 min at $600\,°C$. Major elements were analysed on fused discs diluted 1 (sample):10 (flux mixture) with a Li-tetraborate/Li-metaborate mixture (FX-X65, Fluxana, Kleve, Germany). Pressed powder pellets made of 8 g of air dried sample material were prepared for trace element analysis. The XRF system was equipped with a Pd-tube operated at acceleration voltages between 15 and 53 kV and currents between 1.5 and 12.0 mA. Signal enhancement was achieved for major element analysis by application of secondary targets of Co, Ti, and Al. Trace elements were excited using secondary (Mo, Pd, Co), Barkla (Al_2O_3), and Bragg (HOPG, i.e., highly ordered pyrolytic graphite) targets, respectively, as described by Haschke (1996), and Stephens and Calder (2004). Calculation of element concentrations was done on the basis of 40 certified rock standards. During trace element determination, matrix correction was performed using the Mo-Compton peak. Precisions are <0.9% for the major and <5% for the trace elements, except for Ba (precision <10%). Lower limits of determination are 0.10 wt% for oxides of the major elements, 10 ppm for Zn, 20 ppm for Cr, Ni, Zr, La, Ce, Nb, and 50 ppm for Ba and Cl.

Mineral compositions were determined on polished and carbon-coated thin sections using a JEOL JXA-8900R electron microprobe at the Institute for Applied Mineralogy and Economic Geology, RWTH Aachen University. Operating conditions were 15 KV acceleration voltage and a probe current of 23 nA. For analyses of feldspars, nepheline, sodalite, and cancrinite, a beam diameter of 10 μm was used to avoid errors caused by diffusion of Na. Clinopyroxene and biotite were measured with a beam diameter of 2–3 μm. Natural standards were used to calibrate major and minor elements, measuring times were 10 s on the peak position. The raw data were processed by ZAF corrections.

Element concentrations and isotope compositions of Rb, Sr, Sm, and Nd were determined on powdered whole-rock sample fractions of 30–100 mg. The samples were spiked using ^{87}Rb–^{84}Sr and ^{149}Sm–^{150}Nd mixed spikes before decomposing with HF–HNO_3. For internal Rb–Sr isochrons, 5–20 mg of minerals were separated from two crushed nepheline syenite samples by gravity separation, magnetic enrichment, and a final hand-picking under the binocular microscope before spiking with ^{87}Rb–^{84}Sr spikes and acid decomposition. Rb, Sr, and REE of the

Table 1 Geographical location (UTM), rock type, and chemical composition of Kalkfeld alkaline silicate rock samples (major elements as wt% of the oxides, trace elements in µg/g)

Sample	TK 50	TK 76	TK 98.1	TK 101.1	2009007/2	KF 201#	KF 203#	NJ 480a	NJ 480b	NJ 447	PG 52
UTM coordinates	K33 616252/7695212	K33 617999/7696971	K33 617998/7696879	K33 616200/7695157	K33 615595/7698522	K33 615924/7694081	K33 614092/7698609	K33 615602/7698574	K33 615676/7698574	K33 615585/7698551	K33 614977/7695276
Rock type	NSy	NSy	NSy	NSy	NSy	NSy	NSy	NSys	NSys	NSys	NSye
wt%											
SiO_2	55.19	52.07	50.55	53.75	55.35	54.85	53.63	54.01	53.90	53.07	58.45
TiO_2	0.67	0.68	0.57	0.84	0.71	0.88	0.99	0.75	1.12	0.84	0.15
Al_2O_3	21.17	18.58	19.02	21.95	20.75	21.49	15.85	20.29	17.55	21.50	17.71
Fe_2O_3*	3.33	6.27	5.21	3.31	4.64	3.50	8.55	4.98	7.20	3.82	4.50
MnO	<0.10	0.29	0.29	<0.10	0.14	<0.10	0.33	0.12	0.19	0.10	0.23
MgO	0.41	0.43	0.50	0.44	0.21	0.61	0.54	0.48	0.55	0.49	<0.10
CaO	1.25	2.99	2.56	1.18	0.60	0.34	1.51	1.23	2.28	1.79	2.03
Na_2O	8.11	9.98	8.42	8.50	8.18	6.60	7.53	7.35	7.08	8.64	8.38
K_2O	7.73	6.59	5.39	7.27	7.80	9.41	7.45	8.87	7.46	7.98	4.20
P_2O_5	0.10	0.18	0.22	<0.10	0.10	<0.10	0.12	<0.10	<0.10	<0.10	0.67
LOI	0.75	0.71	6.25	0.93	0.83	1.25**	1.22**	0.74	0.96	1.01	0.87
Total	98.80	98.77	98.98	98.26	99.31	99.04	97.72	98.82	98.35	99.28	97.45
µg/g											
Cr	<20	50	<20	29	<20	11	18	46	33	40	<20
Ni	<20	23	<20	<20	<20	1	2	22	<20	21	32
Zn	49	104	100	50	76	76	198	42	74	38	52
Zr	668	718	741	453	746	351	2215	169	1099	238	14.600*
Nb	197	232	263	271	198	366	436	104	292	125	2400*
Ba	334	718	722	1047	626	679	1073	254	350	1125	121
La	29	86	192	29	22	14	152	33	37	38	506
Ce	60	156	282	62	<50	24	190	61	80	79	689
Cl	nd	149	nd	>1300	nd	450	>1300	>1300	>1300	>1300	nd

Sample	FS 27	TK 70	190907/1	190907/3	190907/4	PG 23	NJ 160	PG 06	PG 25	PG 37	PG 55	FS 04
UTM coordinates	K33 617230/7700118	K33 615602/7696557	K33 613624/7686521	K33 613624/7696521	K33 613532/7696449	K33 615924/7694081	K33 614092/7698609	K33 615602/7693301	K33 617269/7695461	K33 617350/7695803	K33 616724/7695026	K33 617230/7700118
Rock type	NSys	T	T	T	T	T	T	T	T	T	T	T
wt%												
SiO_2	54.50	52.28	55.21	55.23	54.96	56.24	55.59	54.27	54.16	53.48	55.22	53.98
TiO_2	0.82	0.93	0.82	0.69	0.80	0.92	0.86	0.87	0.83	0.83	0.81	0.70
Al_2O_3	20.99	17.88	17.45	19.17	19.01	15.91	17.91	16.87	17.25	18.14	20.68	19.72
Fe_2O_3*	5.27	6.95	7.57	6.35	5.99	8.70	7.62	8.17	7.60	6.94	4.36	5.26
MnO	0.14	0.42	0.30	0.22	0.23	0.34	0.32	0.34	0.31	0.32	0.15	0.20
MgO	0.43	0.60	0.41	0.31	0.40	0.48	0.39	0.34	0.36	0.40	0.30	0.38

Table 1 (continued)

Sample	FS 27	TK 70	190907/1	190907/3	190907/4	PG 23	NJ 160	PG 06	PG 25	PG 37	PG 55	FS 04
UTM coordinates	K33 617230/ 7700118	K33 615602/ 7696557	K33 613624/ 7686521	K33 613624/ 7696521	K33 613532/ 7696449	K33 615924/ 7694081	K33 614092/ 7698609	K33 615602/ 7693301	K33 617269/ 7695461	K33 617350/ 7695803	K33 616724/ 7695026	K33 617230/ 7700118
Rock type	NSys	T	T	T	T	T	T	T	T	T	T	T
CaO	1.13	2.24	1.28	1.01	1.15	1.26	1.23	1.21	1.44	1.79	1.20	1.22
Na$_2$O	8.50	8.48	9.16	7.98	8.32	7.42	8.21	8.77	7.89	8.41	8.46	8.26
K$_2$O	6.98	7.19	6.56	7.58	7.38	6.92	6.65	7.24	7.60	7.45	7.14	7.73
P$_2$O$_5$	<0.10	<0.10	<0.10	<0.10	<0.10	<0.10	<0.10	<0.10	<0.10	<0.10	<0.10	<0.10
LOI	0.26	0.63	0.45	0.27	1.38	0.30	0.88	1.03	1.45	1.91	0.58	1.03
Total	99.06	97.67	99.26	98.81	99.65	98.49	99.74	99.11	98.92	99.67	98.95	98.50
µg/g												
Cr	22	46	47	36	30	42	32	39	<20	<20	46	39
Ni	<20	36	24	<20	23	32	22	25	<20	<20	33	21
Zn	49	256	112	127	127	311	193	153	165	210	91	109
Zr	365	1105	2111	690	1041	803	1809	1512	1458	1225	372	660
Nb	73	389	831	283	362	556	543	466	471	432	256	268
Ba	594	1884	370	274	766	286	412	178	451	747	98	281
La	18	138	268	134	147	299	172	184	195	189	70	54
Ce	<50	188	344	171	201	379	237	250	278	268	122	95
Cl	>1300	251	315	929	716	228	244	>1300	>1300	>1300	>1300	>1300

NSy nepheline syenite, *NSys* sodalite-bearing nepheline syenite, *NSye* eudialyte-bearing nepheline syenite, *T* tinguaite. # chemical data of KF 201, KF 203 from Bühn and Trumbull (2003)

nd not determined

*Total iron given as Fe$_2$O$_3$

**Loss on ignition (LOI) of KF 201 and KF 203 represents the sum of H$_2$O and CO$_2$

whole-rocks samples and the minerals, were separated by the conventional cation exchange techniques using Biorad resin AG 50WX8 and 2.5 N and 6 N HCl. In a second step, Sr was purified on Eichrom Sr spec resin with 3 N HNO_3 as eluent. The separation of Sm and Nd was achieved on HDEHP-coated Teflon powder with 0.17 N and 0.4 N HCl, respectively.

The isotopic composition of Rb was determined on a VG sector 54 multi-collector mass spectrometer operated in a static mode, the isotope compositions of Sr, Sm, and Nd on a Triton multi-collector spectrometer operated in dynamic mode. Double filament techniques were applied to Rb (loaded with H_2O on Ta), and Sm and Nd (both loaded with H_3PO_4 on Re). Sr was loaded with TaF_5 on a central W filament. Rb isotope ratios were corrected for mass fractionation using a factor deduced from multiple measurements of Rb standard reference material NBS 607, the isotopic fractionations of Sr and Nd were corrected by normalization of the measured data to $^{86}Sr/^{88}Sr = 0.1194$ and $^{146}Nd/^{144}Nd = 0.7219$, respectively. During the period of study, repeated measurement of standards resulted in the following means and 2σ errors: NBS SRM 607: $^{85}Rb/^{87}Rb = 2.6035$ ($n=2$); NBS SRM 987: $^{87}Sr/^{86}Sr = 0.710200 \pm 26$ ($n=9$); La Jolla Nd Standard: $^{143}Nd/^{144}Nd = 0.511848 \pm 15$ ($n=6$). Total blanks did not exceed 50 pg Rb, 100 pg Sr, 50 pg Sm, and 200 pg Nd. All mass spectrometric measurements were performed at the Institute of Mineralogy, University of Münster.

Rb–Sr isochrons were calculated according to Ludwig (2003) on a 1 σ-level and a 1.5% error on the $^{87}Rb/^{86}Sr$ ratios. The initial ε_{Sr} and ε_{Nd} values were calculated at 242 Ma using the decay constants $\lambda\ ^{87}Rb = 1.42 \times 10^{-11}$ a^{-1} (Steiger and Jäger 1977) and $\lambda\ ^{147}Sm = 6.54 \times 10^{-12}\ a^{-1}$ (Lugmair and Marti 1978), respectively.

Results

Petrography and mineral chemistry

Alkali feldspar and nepheline are the dominant components of the nepheline syenites, and clinopyroxene and biotite are present in minor amounts in this rock type. Euhedral to subhedral platy crystals of alkali feldspar reach up to 1 cm in length, but most crystals are smaller and form the ground mass of the rocks. All feldspar crystals show extensive perthitic exsolution into nearly pure albite and a K-rich alkali feldspar (Fig. 2a; Table 2). Furthermore, vein-perthitic alterations of the mineral are likewise common. For nepheline syenite sample TK 101.1, bulk compositions of the perthitic feldspar, obtained from integrating electron microprobe measurements using a defocused beam with a diameter of 10 μm, show the range $Or_{49-86}Ab_{14-51}Cls_{0-2}$.

In general, BaO concentrations decrease from the center towards the crystal margins from >2 to <0.1 wt%. The compositional variation is illustrated in Fig. 3 and representative analyses are given in Table 2.

During a late stage of magmatic crystallization, a second type of potassic feldspar is formed in the nepheline syenites by decomposition of biotite. This feldspar is intimately intergrown with magnetite and titanite (Fig. 2a, b). Its grain size does not exceed 30 μm. The magnetite is characterized by grain sizes up to 100 μm. Ilmenite exsolution lamellae within these crystals is a typical feature (Fig. 2b).

In contrast to the nepheline syenites, feldspar in the fine grained tinguaites occurs as individual crystals of both albite and alkali feldspar (Fig. 2c). These feldspars are free from perthitic exsolutions and mutually show very limited solid solutions (Table 2), suggesting crystallization under sub-solvus conditions. Rare alkali feldspar phenocrysts of this rock type locally contain perthitic relics, which are reminiscent of feldspar from nepheline syenite.

Nepheline shows a very limited variation in chemical composition within individual samples and over the whole suite of analysed rocks (Table 2). The variability spans the range $Ne_{69-72}Ks_{18-22}Q_{9-12}$. Contents of Fe_2O_3 and CaO are <1 and <0.1 wt%, respectively. Small-scale lobate intergrowth textures between nepheline and clinopyroxene grains, as shown in Fig. 2a, are likewise a typical feature of this rock type.

During the late stages of magmatic crystallization of the nepheline syenites and commonly near the locations of biotite decomposition, the nepheline crystals are partly dissolved and replaced by cancrinite (Fig. 2d).

Clinopyroxene is a common constituent of all samples. It forms long-prismatic to needle-like euhedral and chemically homogeneous crystals in the tinguaites (Fig. 2c), but anhedral grains with chemically heterogeneous central parts in the nepheline syenites (Fig. 2a). Very fine grained needles of clinopyroxene can exclusively be observed in nepheline crystals of nepheline syenite samples. Such formation has been explained as product of late-stage exsolution by Woolley et al. (1996). In the tinguaites, the chemical variability of clinopyroxene is confined to compositions with high Na contents and thus an aegirine component >60 Mol% (Fig. 4). This clinopyroxene is classified as aegirine or aegirine-augite (Morimoto et al. 1988). High Ti concentrations of more than 5 wt% in parts of the crystals suggest the presence of a major "neptunite" component (Ferguson 1977) ranging to >30 mol%. In nepheline syenites, the clinopyroxene composition spans an overall range from $Ac_1Di_{73}Hd_{26}$ to $Ac_{89}Di_6Hd_5$. Individual crystals show a patchy distribution of chemical components. Representative chemical analyses are presented in Table 3.

The subhedral platy crystals of biotite reach 2 mm in length in the nepheline syenites and 300 μm in the
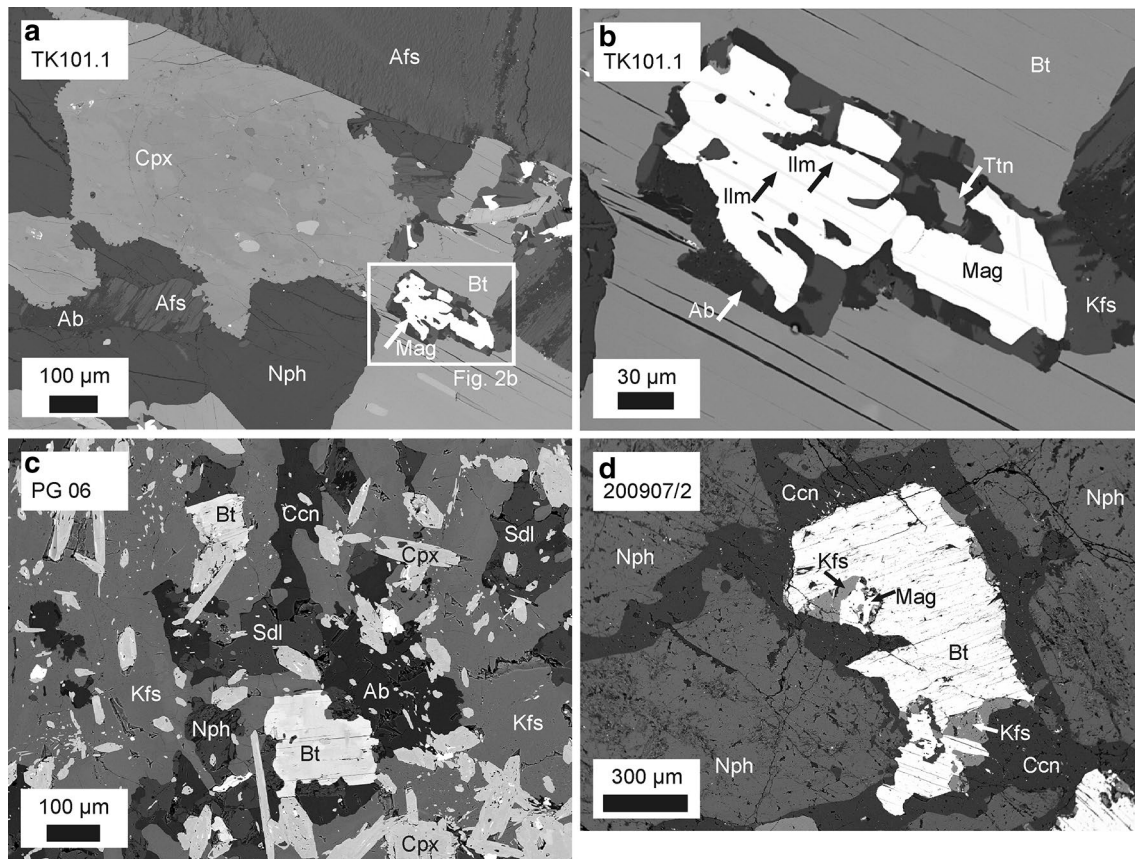
Fig. 2 Back-scattered electron images of mineral textures from Kalkfeld nepheline syenites and tinguaites. *Sample numbers* shown in the *upper left corner. Ab* albite, *Afs* alkali feldspar, *Bt* biotite, *Ccn* cancrinite, *Cpx* clinopyroxene, *Ilm* ilmenite, *Kfs* potassic feldspar, *Mag* magnetite, *Np*h nepheline, *Sdl* sodalite, *Ttn* titanite (abbreviations according to Whitney and Evans 2010), **a** nepheline syenite TK 101.1: Afs shows perthitic exsolutions, Bt is partially decomposed into the association potassic feldspar–magnetite–titanite, Cpx is char-acterized by a patchy back-scatter electron intensity in the central part of the crystal, its margins finger with a lobate texture into the Nph crystals on a small scale, **b** enlargement of the area of Bt decomposition from (**a**), Mag shows Ilm exsolution lamellae; **c** tinguaite PG 06: Euhedral and subhedral Cpx and Bt in a silicate matrix of Afs, Ab, Sdl, and Ccn; **d** nepheline syenite 200907/2: Ccn replaces dissolving Nph crystals in the surrounding of decomposing Bt

tinguaites. In both rock types, they are commonly associated with clinopyroxene grains and form clusters with diameters of several millimetres. In some tinguaite samples, biotite is partly replaced by clinopyroxene, in others, biotite has overgrown the clinopyroxene crystals. Chemically, biotite is fairly homogeneous over all samples. Representative compositions are given in Table 4. Decomposition embayments along the crystal surfaces during late magmatic stages and the local replacement by potassic feldspar–magnetite–titanite associations were repeatedly observed in the nepheline syenites (Fig. 2a, b, d).

Individual cancrinite and sodalite crystals, the latter with 5–6 wt% Cl, are minor components of the ground mass in tinguaite samples. In these samples, rare crystals of eudialyte, zircon, and chevkinite show a poikilitic character indicative of a late-stage magmatic formation. Fluorite is found as a very rare component.

Major and trace element compositions of whole-rock samples

Major and most trace elements of the nepheline syenite and tinguaite samples show a limited variation of concentration (Table 1). The SiO_2 concentrations range from 50.55 to 58.45 wt%; for all samples, the sum of Na_2O and K_2O exceeds 14.30 wt%. The samples are peralkaline with molar $(Na+K)/Al$ ranging from 1.00 to 1.32; the Si/Al ratio is between 2 and 3. CaO and MgO concentrations do not exceed 3.00 and 0.60 wt%, respectively. Concentrations of P_2O_5 are low (<0.1 wt%); only sample PG 52 is an exception with 0.67 wt% P_2O_5. Incompatible trace elements can be highly enriched in individual samples (Table 1), e.g., 14,600 µg/g Zr in sample PG 52. The Rb concentrations range between 106 and 241 µg/g; Sr concentrations vary between 907 and 5671 µg/g (Table 5). Altogether, the analysed samples correspond chemically very closely

Table 2 Representative single spot electron microprobe analyses of alkali feldspar and nepheline from Kalkfeld nepheline syenites and tinguaites

Sample	TK101.1	TK101.1	TK101.1	TK101.1	200907/2	200907/2	PG06	PG06
Rock type	NSy	NSy	NSy	NSy	NSy	NSy	T	T
Mineral	Afs, Xc	Afs, Xm	Kfs, Bi dec.	Ab, perth.	Afs, Xc	Afs, Xm	Kfs	Ab
Wt%								
SiO_2	64.61	65.53	64.06	67.18	64.45	64.19	64.23	67.95
Al_2O_3	19.22	18.99	18.05	19.13	19.68	18.98	18.80	20.34
$Fe_2O_3{}^{\#}$	0.18	0.32	0.67	0.34	0.24	0.20	0.52	0.20
CaO	0.02	0.00	0.00	0.02	0.00	0.00	0.00	0.01
BaO	0.70	0.10	0.00	0.15	1.29	0.46	0.01	0.00
Na_2O	4.37	5.85	1.28	11.20	4.62	1.02	0.75	10.73
K_2O	10.22	8.54	15.11	0.41	9.40	15.22	15.52	0.12
Total	99.32	99.33	99.17	98.43	99.68	100.07	99.83	99.35
8 oxygens p.f.u								
Si	2.963	2.976	2.985	2.990	2.947	2.968	2.972	2.977
Al	1.039	1.016	0.991	1.000	1.061	1.034	1.025	1.050
Fe^{3+}	0.006	0.011	0.023	0.011	0.008	0.007	0.018	0.007
Ca	0.001	0.000	0.001	0.000	0.000	0.000	0.000	0.000
Ba	0.012	0.002	0.000	0.003	0.023	0.008	0.000	0.000
Na	0.389	0.515	0.115	0.967	0.410	0.091	0.067	0.912
K	0.598	0.495	0.899	0.024	0.548	0.898	0.916	0.007
Total	5.008	5.015	5.013	4.995	4.997	5.006	4.998	4.953
Mol%								
Cls	1	0	0	0	2	1	0	0
Ab	39	51	11	97	42	9	93	1
Kfs	60	49	89	3	56	90	7	99

Sample	TK101	200907/2	PG06	NJ160
Rock type	NSy	NSy	T	T
Mineral	Neph	Neph	Neph	Neph
Wt%				
SiO_2	43.12	43.84	41.76	44.01
Al_2O_3	33.30	33.22	35.11	33.20
$Fe_2O_3{}^{\#}$	0.87	0.74	0.33	0.76
CaO	0.00	0.00	0.02	0.03
BaO	0.05	0.00	0.00	0.00
Na_2O	16.04	16.17	14.94	16.76
K_2O	6.36	6.10	7.14	6.26
Total	99.74	100.07	99.30	101.02
32 oxygens p.f.u				
Si	8.326	8.410	8.097	8.453
Al	7.578	7.511	8.025	7.517
Fe^{3+}	0.127	0.107	0.049	0.111
Ca	0.000	0.000	0.003	0.005
Ba	0.004	0.000	0.000	0.000
Na	6.006	6.014	5.616	5.881
K	1.567	1.493	1.767	1.537
Total	23.608	23.535	23.557	23.504
Mol%				
Neph	72	71	69	70

Table 2 (continued)

Sample	TK101	200907/2	PG06	NJ160
Rock type	NSy	NSy	T	T
Mineral	Neph	Neph	Neph	Neph
Kls	19	18	22	18
Qz	9	11	9	12

Rock types according to Table 1, abbreviations of mineral names after Whitney and Evans (2010), *Xc* crystal core, *Xm* crystal margin

[#]Total iron given as Fe_2O_3

Fig. 3 Compositions of feldspar for Kalkfeld nepheline syenite samples TK 101.1 and 200907/2, and the tinguaite sample PG 06 within the variation diagram orthoclase–albite–celsian (Or–Ab–Cls). For nepheline syenites, the alkali feldspar compositions of crystal centers and margins are distinguished (*Afs* alkali feldspar, *X* crystal) as well as potassic feldspar formed by decomposing biotite (Kfs, bio dec.). Albite (Ab) composition of this rock type was measured in vein-perthitic enrichments (perth. vein). For tinguaite sample PG 06, the composition of rare phenocrysts is shown separated from the groundmass feldspars


Rb–Sr and Sm–Nd isotope data

The $^{87}Rb/^{86}Sr$ and $^{87}Sr/^{86}Sr$ ratios of the nepheline syenite and tinguaite samples (Table 5) show a systematic positive covariation. Together with the data of two Kalkfeld carbonatite samples published by Le Roex and Lanyon (1998), the $^{87}Rb/^{86}Sr$–$^{87}Sr/^{86}Sr$ pairs define a regression line corresponding to a date of 240.0 ± 9.2 Ma (1 σ confidence level) with a mean square weighted deviation (MSWD) of 9.4. The line intersects the $^{87}Sr/^{86}Sr$-axis at 0.703737 ± 0.000043 (Fig. 5a). The data of the two types of silicate rocks are distributed along this line. The $^{87}Rb/^{86}Sr$ ratios of the samples show a little variation and range from 0.0694 to 0.7037. Consequently, the

to compositions as reported by Trumbull et al. (2000) and Bühn and Trumbull (2003) for nepheline syenites and foidites of the complex.

regression line is poorly constrained. The Sr isotopic data of the individual samples calculated for 240 Ma show no systematic relationship to the respective Sr concentrations (Fig. 5b), which excludes an interpretation of the regression line in Fig. 5a as a mixing line between two components different in Sr concentration and Sr isotopic composition.

Mineral Rb–Sr isotope investigations were done on separated minerals of the coarse-grained nepheline syenite samples TK 101.1 and 200907/2. The results are listed in Table 6. Each set of mineral data defines an isochron with a slope corresponding to 242.3 ± 4.8 and 242.4 ± 6.5 Ma (1 σ), respectively (Figs. 6, 7). Both dates are essentially fixed by the highly radiogenic biotites. For the two isochrons, MSWD values are 0.34 and 3.2, respectively. Within the limits of error, the initial $^{87}Sr/^{86}Sr$ ratios of these isochrons are identical to the intersection of the whole-rock regression line with the $^{87}Sr/^{86}Sr$ axis.
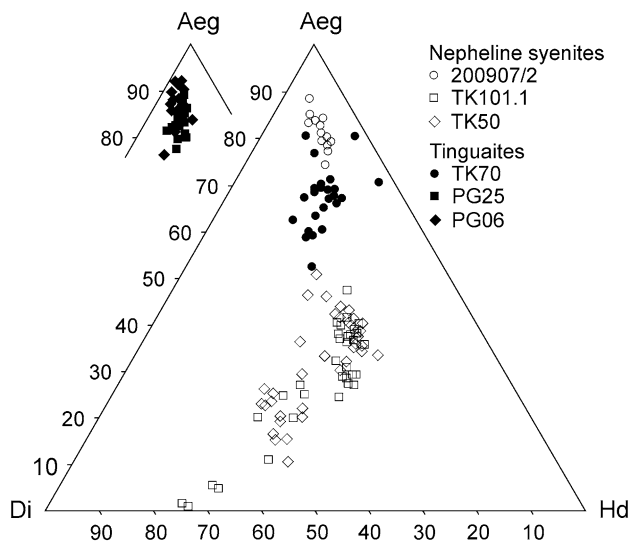
Fig. 4 Clinopyroxene compositions of the Kalkfeld nepheline syenites and tinguaites are shown in the variation diagram aegirine–diopside–hedenbergite (Aeg–Di–Hd). Calculation of the end member compositions is given in Table 4

Samarium and Nd concentrations of the whole-rock silicate samples vary from 0.8 to 26.2 and 6.2 to 166.3 μg/g, respectively (Table 5). The $^{147}Sm/^{144}Nd$ ratios cluster around 0.09 for most samples, only the tinguaite samples PG 23 and 190907/3 have distinctly lower ratios of 0.036 and 0.059, respectively. The measured $^{143}Nd/^{144}Nd$ ratios range from 0.512499 to 0.512610. This range includes data for Kalkfeld silicate rocks published by Bühn and Trumbull (2003) as well as those given for carbonatite samples by Trumbull et al. (2000).

Discussion and conclusions

While some mineralogical features (i.e., celsian bearing feldspar cores and aegirine poor cores of clinopyroxene crystals) point to early crystallization stages of the Kalkfeld nepheline syenites, petrographic investigations on the samples show also that three of the dominant mineral species, i.e., alkali feldspar, nepheline, and biotite, experienced late alterations. For the perthitization of feldspar, the time of alteration is hard to deduce. The local decomposition of biotite to alkali feldspar, magnetite, and titanite with grain sizes up to 100 μm, however, documents a high-temperature *in situ* crystallization process. This is in line with the observation of biotite decomposition in embayments along the grain margins and a lack of fine grained crystalline alterations along cleavage planes. Replacement of nepheline by cancrinite (ideal structural formula $Na_6Ca_2[Al_6Si_6O_{24}](CO_3)_2 + nH_2O$, Sirbescu and Jenkins 1999) indicates a decomposition process mediated by a

CO_2 dominated fluid. Further evidence of elevated temperatures during this alteration is the formation of cancrinite in larger domains (>200 μm) forming a network in the inter-crystalline space of nepheline crystals. Experimental studies show that growth of cancrinite critically depends on the presence of H_2O in the fluid next to CO_2 (Sirbescu and Jenkins 1999). The textural association of cancrinite with biotite suggests decomposition of the latter as the plausible source of H_2O. In conclusion, the petrographical observations document a high temperature and thus late magmatic fluid mediated reworking of the initial mineral association biotite, alkali feldspar, clinopyroxene, and nepheline. The two internal isochrons from the Kalkfeld nepheline syenite samples, which are defined by these mineral phases, are interpreted to date this late magmatic crystallization at 242 ± 6.5 Ma (using the larger of the two isochron errors). From the subvolcanic level and the limited size of the intrusion, it is inferred that the late magmatic process and the intrusion age of the magma are identical within the 6 Ma uncertainty.

The slope of the regression line calculated from the whole-rock isotope values yields a date (240 ± 9.2 Ma), which is identical within limits of error to the ages of the mineral isochrons. This argues for a fairly homogeneous distribution of Sr isotope compositions among the nepheline syenites and tinguaites including the carbonatites exposed in the central plug of the complex (samples K 2 and K 22, see Fig. 5a). It is in line with the assumption of a short event comprising formation, ascent, shallow intrusion, and crystallization of magmas.

Based on the well-defined mineral isochrons, the age of 242 ± 6.5 Ma is applied for further calculation. At 242 Ma, the initial $^{87}Sr/^{86}Sr$ and $^{143}Nd/^{144}Nd$ ratios of the whole-rock silicate samples correspond to ε_{Sr} of -9.7 ± 0.8 and to ε_{Nd} varying between $+1.6$ and $+2.5$ (Table 5). The Sr isotope data of Kalkfeld samples reported by Ziegler (1992), Le Roex and Lanyon (1998), Trumbull et al. (2000), and Bühn and Trumbull (2003) also fall into this span, when recalculated to ε_{Sr} at 242 Ma, which is a significantly reduced variation compared to the calculations assuming 130 Ma (e.g. Bühn and Trumbull 2003). In the case of ε_{Nd}, only sample K 2 reported by Le Roex and Lanyon (1998) fits that range. In a ε_{Sr} vs. ε_{Nd} plot, all data are in the depleted quadrant indicating a source with a time-integrated depletion in LIL elements (Fig. 8). Based on the Nd-Sr isotope data, at 242 Ma, a common, isotopically homogeneous source for the Kalkfeld nepheline syenites, tinguaites, and carbonatites, and thus, a common melt evolutionary history can be suggested for the complex (cf. Bühn and Trumbull 2003).

Middle Triassic magmatic activity is a rare feature for southern Africa and so far unknown for the northwestern part of Namibia. There are a few occurrences of kimberlite

Table 3 Representative microprobe analyses of clinopyroxene from Kalkfeld nepheline syenites and tinguaites

Sample	TK101.1	TK101.1	200907/2	200907/2	TK50	PG06	TK70	NJ160
Rock type	NSy, Xc	NSy Xm	NSy	NSy	NSy	T	T	T
Wt%								
SiO_2	51.35	51.18	52.46	52.51	52.40	53.23	51.59	52.48
TiO_2	0.82	0.60	0.49	0.52	0.27	1.66	0.25	3.65
Al_2O_3	1.65	1.04	1.30	1.30	0.93	1.36	1.02	1.21
$Fe_2O_3^{\#}$	4.39	12.15	25.50	25.62	6.58	23.37	19.91	18.57
FeO	7.84	10.43	3.95	3.91	9.48	4.39	4.84	6.57
MnO	0.57	0.77	0.24	0.28	0.71	0.60	1.78	0.74
MgO	10.44	3.95	1.23	1.19	7.83	1.20	3.08	1.26
CaO	21.60	13.93	2.99	3.69	18.59	2.19	9.04	4.28
Na_2O	1.60	5.53	11.42	11.26	3.23	11.91	8.24	10.99
Total	100.26	99.58	99.58	100.28	100.02	99.91	99.75	99.75
Formulae based on 4 cations and 6 oxygens								
Si	1.937	1.989	2.013	2.005	1.996	2.026	1.989	2.008
Ti	0.023	0.018	0.014	0.015	0.008	0.048	0.007	0.105
Al	0.073	0.048	0.059	0.058	0.042	0.061	0.046	0.054
Fe^{3+}	0.125	0.355	0.736	0.736	0.189	0.669	0.578	0.535
Fe^{2+}	0.247	0.339	0.127	0.125	0.302	0.140	0.156	0.210
Mn	0.018	0.025	0.008	0.009	0.023	0.019	0.058	0.024
Mg	0.587	0.229	0.070	0.068	0.444	0.068	0.177	0.072
Ca	0.873	0.580	0.123	0.151	0.759	0.089	0.373	0.176
Na	0.117	0.417	0.850	0.833	0.238	0.879	0.616	0.816
Total	4.000	4.000	4.000	4.000	4.001	3.999	4.000	4.000
End members (Mol%)								
Jd	7	5	6	6	4	6	5	6
Aeg	5	36	74	74	19	67	57	54
Di	59	23	7	7	44	7	18	7
Hd	26	35	5	8	31	2	19	10
Nept	0	1	3	3	1	10	0	21
Fs	0	0	0	0	0	4	0	1
Rest	3	0	5	2	0	4	1	1
Total	100	100	100	100	99	100	100	100
Σ Aeg + Di + Hd (Mol%)	90	94	86	89	95	75	94	71
Aeg	5	38	86	83	20	88	60	75
Di	66	24	8	8	47	9	19	10
Hd	29	38	6	9	33	3	21	15
Total	100	100	100	100	100	100	100	100

Clinopyroxene end members have been calculated in the sequence jadeite (=Al), aegirine (=Fe^{3+}), diopside (=Mg), hedenbergite (=Ca rest after subtraction of the portion for diopside), neptunite (Na rest after subtraction of the portions for jadeite and aegirine), ferrosilite (rest of Fe^{2+} + Mn). $Fe_2O_3^{\#}$ calculated according to Droop (1987) from total iron measured as FeO

NSy nepheline syenite, *T* tinguaite, *Xc* crystal core, *Xm* crystal margin

in Botswana dated at 235 ± 2 Ma (Kinny et al. 1989). For the Paraná-Etendeka Province, emplacement ages of ~240 Ma have so far only been reported from its westernmost margins in South America (Alto Paraguay), namely the sodic alkaline complexes of Cerro Boggiani and Cerro Siete Cabezas (Gomes et al. 1996; Comin-Chiaramonti et al. 2007a, b). The Kalkfeld alkali silicate–carbonatite

volcanism predates the Karoo volcanic event, which dates for the northern Karoo extrusions at 178–182 Ma (Jourdan et al. 2005), by about 60 Ma. The Early Cretaceous Parana–Etendeka event as well as the emplacement of the numerous Damaraland ring complexes including Brandberg, Messum, and Okenyenya are predated by more than 100 Ma. In addition, the nepheline syenites of the Etaneno

Table 4 Representative microprobe analyses of biotite from Kalkfeld nepheline syenites and tinguaites

Sample	TK101.1	TK101.1	200907/2	200907/2	NJ447	PG06	NJ160	TK70
Rock type	NSy	NSy	NSy	NSy	NSys	T	T	T
Wt%								
SiO_2	34.74	36.22	35.85	35.63	36.56	36.24	35.62	35.23
TiO_2	5.18	4.82	4.46	5.21	3.90	2.42	3.73	2.46
Al_2O_3	11.82	11.67	10.42	11.61	10.41	11.44	11.41	11.58
$FeO^#$	25.33	25.24	26.82	27.45	25.66	24.09	29.18	24.50
MnO	0.98	0.56	1.08	0.99	1.01	4.20	2.05	3.94
MgO	8.39	8.71	6.95	6.53	8.90	6.81	4.96	7.33
CaO	0.00	0.00	0.02	0.00	0.00	0.00	0.03	0.00
Na_2O	0.16	0.20	0.20	0.19	0.21	0.10	0.14	0.14
K_2O	9.63	9.77	9.49	9.60	9.74	9.87	9.31	9.65
Cl	0.00	0.00	nd	nd	0.01	0.00	0.02	0.00
F	0.34	0.67	0.96	0.75	0.70	0.78	0.62	0.97
−O for F, Cl	−0.14	−0.29	−0.40	−0.32	−0.30	−0.33	−0.26	−0.41
Total	96.43	97.56	95.85	97.64	96.80	95.61	96.81	95.39
22 oxygens p.f.u								
Si	5.478	5.597	5.702	5.573	5.724	5.785	5.694	5.650
Ti	0.614	0.560	0.534	0.613	0.459	0.291	0.449	0.296
Al	2.197	2.126	1.953	2.140	1.922	2.152	2.149	2.188
Fe^{2+}	3.340	3.262	3.567	3.591	3.360	3.215	3.901	3.286
Mn	0.131	0.073	0.145	0.131	0.133	0.568	0.227	0.535
Mg	1.972	2.008	1.648	1.523	2.078	1.621	1.881	1.753
Ca	0.000	0.000	0.003	0.000	0.000	0.000	0.005	0.000
Na	0.047	0.059	0.062	0.058	0.063	0.031	0.042	0.042
K	1.937	1.925	1.926	1.916	1.945	2.010	1.898	1.974
Total cations	15.716	15.610	15.540	15.545	15.684	15.671	15.597	15.724

NSy nepheline syenite, *NSys* sodalite-bearing nepheline syenite, *T* tinguaite, *nd* not determined

$^#$Total iron given as FeO

Complex, situated within 15 km of the Kalkfeld Complex, intruded more than 100 Ma later (i.e. 134 ± 3 Ma, Müller 1996) than the Kalkfeld rocks.

The Pan-African Damara Orogenic Belt with its marked SW–NE striking structures and shear zones represents a zone of protracted crustal weakness (e.g. Martin et al. 1960; Marsh 1973; Milner et al. 1995; Trumbull et al. 2000, 2003, 2004). A first reactivation of its shear zones connected with a rift formation occurred during Permo-Triassic times when first Karoo basins were formed (Hegenberger 1988; Daly et al. 1989; Lambiase 1989; Binks and Fairhead 1992; Stollhofen 1999; Wanke and Stollhofen 2000). Onset of subsidence and sedimentation in the Waterberg–Erongo area is associated with tectonic activity of the Waterberg–Omaruru Fault zone in the late Early Triassic close to the crustal segment hosting the Kalkfeld intrusion (Holzförster et al. 1998). The new age data for Kalkfeld indicate that the complex intruded during this first phase of structural reactivation, and we suggest that during this time, shear zones served as pathways for the uprising alkaline melts.

After a period of about 100 Ma of tectonic quiescence following the Early Triassic, a second phase of reactivation started with extension tectonics and crustal thinning. The pre-magmatic period of this reactivation phase is variously estimated at from about 10 Ma (Jerram et al. 1999) to about 25 Ma (Gladczenko et al. 1997) before the 130 Ma emplacement of the Damaraland Early Cretaceous alkaline complexes (e.g., Milner et al. 1995; Schmitt et al. 2000; Wigand et al. 2004). Also, for this Cretaceous time, shear zones are interpreted to represent the pathways for the ascending magmas (e.g., Martin et al. 1960; Marsh 1973; Harry and Sawyer 1992; Milner et al. 1995; Trumbull et al. 2000, 2003). The spatially closely related Triassic Kalkfeld and the Cretaceous Damaraland complexes thus document the repeated intrusions of alkaline and carbonatitic melts along an old lithospheric lesion. It should be stressed that several tectono-magmatic cases are documented showing repeated ascent of mantle-derived alkaline and carbonatite melts along repeatedly activated fault zones, e.g., at the Rungwe intersection of the East African Rift System (Bailey 1992, 1993; Bailey and Woolley 1999). This raises

Table 5 Rb–Sr and Sm–Nd isotope data of Kalkfeld nepheline syenite and tinguaite whole-rock samples

Sample	Rb (µg/g)	Sr (µg/g)	$\frac{^{87}Rb}{^{86}Sr}$	$\frac{^{87}Sr}{^{86}Sr}$	$\frac{^{87}Sr}{^{86}Sr}$ at 242 Ma	εSr at 242 Ma	Sm (µg/g)	Nd (µg/g)	$\frac{^{147}Sm}{^{144}Nd}$	$\frac{^{143}Nd}{^{144}Nd}$	$\frac{^{143}Nd}{^{144}Nd}$ at 242 Ma	εNd at 242 Ma
TK 50	175.4	1287	0.3943	0.705007 ± 23	0.703650	−10.8	2.89	19.07	0.0917	0.512597 ± 7	0.512452	2.5
TK 76	115.3	1899	0.1756	0.704349 ± 13	0.703745	−9.4	6.92	51.94	0.0809	0.512570 ± 5	0.512442	2.3
TK 98.1	106.6	1711	0.1802	0.704395 ± 14	0.703775	−9.0	9.89	75.32	0.0794	0.512581 ± 6	0.512455	2.5
TK 101.1	187.8	1674	0.3244	0.704819 ± 15	0.703702	−10.0	3.14	20.55	0.0925	0.512595 ± 11	0.512448	2.4
2009077/2	207.6	989	0.6072	0.705760 ± 12	0.703670	−10.5	1.65	10.18	0.0979	0.512610 ± 13	0.512455	2.5
KF 201	233.0	958	0.7037	0.706142 ± 13	0.703720	−9.8	0.97	6.64	0.0881	0.512580 ± 8	0.512440	2.2
KF 203	173.9	4239	0.1186	0.704128 ± 14	0.703720	−9.8	8.11	54.76	0.0896	0.512576 ± 8	0.512434	2.1
NJ 480a	211.5	1253	0.4883	0.705440 ± 15	0.703759	−9.2	2.11	15.79	0.0807	0.512562 ± 7	0.512434	2.1
NJ 480b	169.9	907	0.5419	0.705665 ± 12	0.703800	−8.6	4.03	25.25	0.0965	0.512600 ± 6	0.512447	2.4
NJ 447	169.3	1474	0.3323	0.704846 ± 14	0.703702	−10.0	4.16	28.96	0.0869	0.512569 ± 8	0.512431	2.0
PG 52	136.1	5671	0.0694	0.704056 ± 12	0.703817	−8.4	26.19	166.27	0.0952	0.512559 ± 7	0.512408	1.6
FS 27	207.2	1287	0.4659	0.705350 ± 14	0.703746	−9.4	0.81	6.19	0.0792	0.512558 ± 15	0.512433	2.1
TK 70	173.1	3426	0.1461	0.704124 ± 13	0.703621	−11.2	7.73	49.20	0.0950	0.512597 ± 6	0.512447	2.4
1909077/1	230.0	3090	0.2153	0.704412 ± 15	0.703671	−10.5	9.21	71.56	0.0778	0.5125727	0.512449	2.4
1909077/3	208.8	1998	0.2993	0.704719 ± 14	0.703689	−10.2	2.78	28.49	0.0590	0.512529 ± 11	0.512436	2.1
1909077/4	143.1	2662	0.1554	0.704239 ± 12	0.703704	−10.0	5.20	41.17	0.0764	0.512565 ± 3	0.512444	2.3
PG 23	240.5	2095	0.3321	0.704900 ± 13	0.703757	−9.2	3.27	54.35	0.0364	0.512499 ± 8	0.512441	2.2
NJ 160	228.6	2329	0.2840	0.704698 ± 15	0.703720	−9.8	5.49	44.94	0.0739	0.512547 ± 12	0.512430	2.0
PG 06	190.2	2691	0.2045	0.704406 ± 12	0.703702	−10.0	7.72	54.77	0.0852	0.512582 ± 5	0.512447	2.4
PG 25	176.6	2880	0.1774	0.704480 ± 15	0.703869	−7.7	8.42	60.93	0.0835	0.512575 ± 5	0.512443	2.3
PG 37	209.4	2899	0.2089	0.704464 ± 14	0.703745	−9.4	8.43	60.35	0.0845	0.512573 ± 5	0.512439	2.2
PG 55	199.7	1162	0.4970	0.705467 ± 14	0.703756	−9.3	4.88	35.16	0.0839	0.512576 ± 8	0.512443	2.3
FS 04	198.0	1526	0.3754	0.705002 ± 13	0.703710	−9.9	3.21	23.35	0.0830	0.512570 ± 8	0.512439	2.2
K-2*				0.703761 ± 21	0.703731	−9.7	184	1566	0.0710	0.512528	0.512416	1.7
K-22*				0.703716 ± 13	0.703716	−9.9	391	2424	0.0975	0.512518	0.512364	0.7

Initial ε_{Sr} and ε_{Nd} values at 242 Ma were calculated using $(^{87}Sr/^{86}Sr)_{UR} = 0.7047$, $(^{87}Rb/^{86}Sr)_{UR} = 0.0847$ and $(^{143}Nd/^{144}Nd)_{CHUR} = 0.512638$, $(^{147}Sm/^{144}Nd)_{CHUR} = 0.1967$, respectively

*Rb–Sr and Sm–Nd isotope data of Kalkfeld carbonatite samples K 2 and K 22 from Le Roex and Lanyon (1998).
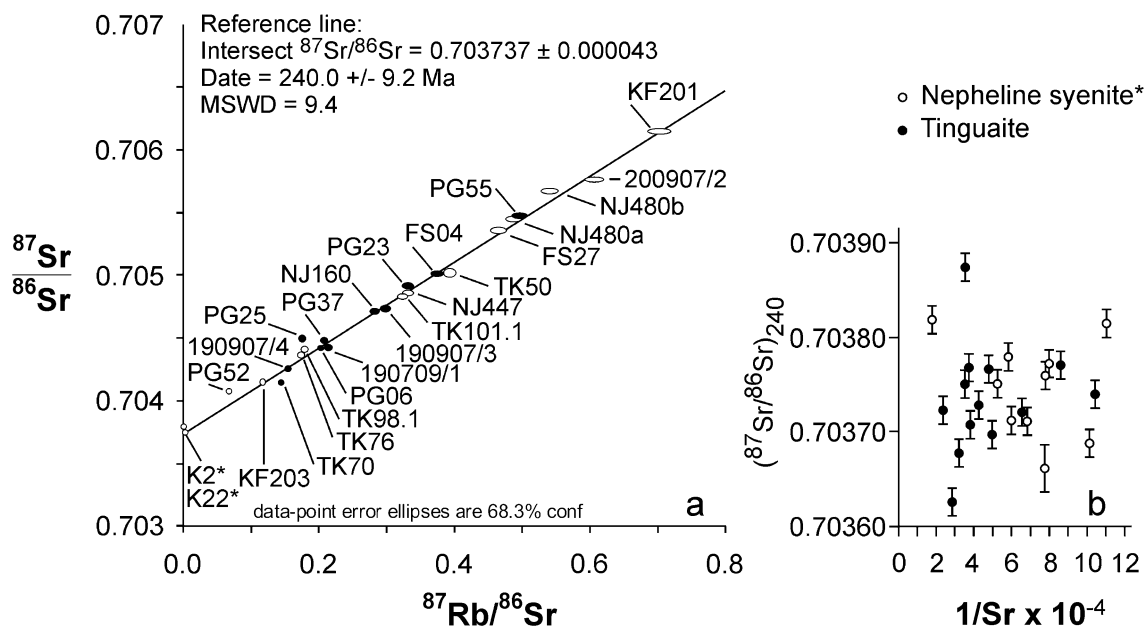
Fig. 5 a Rb–Sr whole-rock isotope data of nepheline syenites (*open symbols*) and tinguaites (*closed symbols*) from Kalkfeld. The asterix marks isotope data for the two carbonatite samples K 2 and K 22 (*open symbols*) from Le Roex and Lanyon (1998). The reference line, the date according to its slope, and the intersect with the ^{87}Sr/^{86}Sr-axis are calculated using Isoplot 3.00 (Ludwig 2003). **b** (^{87}Sr/^{86}Sr)$_{240}$ vs. 1/Sr plot indicates no systematic correlation for the Kalkfeld silicate samples

Table 6 Rb–Sr isotope data of minerals separated from Kalkfeld nepheline syenite samples 200907/2 and TK 101.1

| Sample	Mineral	Grain size fraction (µm)	Rb (µg/g)	Sr (µg/g)	^{87}Rb/^{86}Sr	^{87}Sr/^{86}Sr
200907/2	Feldspar	180–250	192.8	1143.2	0.4879	0.705411 ± 14
	Feldspar	250–500	167.3	801.0	0.6041	0.705810 ± 12
	Clinopyroxene	180–250	15.14	298.0	0.1470	0.704260 ± 12
	Nepheline	250–500	180.1	546.7	0.9561	0.707189 ± 12
	Biotite	180–250	825.1	11.683	219.17	1.449491 ± 57
	Biotite	250–500	769.6	6.684	375.54	2.009616 ± 47
	Whole-rock		207.6	989.0	0.6072	0.705760 ± 12
TK 101.1	Feldspar	100–125	177.0	1767.6	0.2896	0.704685 ± 34
	Feldspar	125–180	183.1	1860.4	0.2847	0.704691 ± 15
	Clinopyroxene	100–125	31.20	766.3	0.1178	0.704120 ± 17
	Clinopyroxene	125–180	41.89	816.9	0.1483	0.704215 ± 14
	Biotite	100–125	832.9	21.45	116.69	1.101825 ± 87
	Biotite	125–180	741.9	20.13	110.63	1.089756 ± 48
	Whole-rock		187.8	1674.0	0.3244	0.704819 ± 15

the question of how similar or different were the sources of Kalkfeld and the Damaraland Alkaline Complexes.

Alkaline and basic igneous rocks and carbonatites of the Cretaceous Damaraland Complexes, e.g., nepheline syenites of Messum (Harris et al. 1999), nephelinites and sövites of Okorusu (Le Roex and Lanyon 1998), and lamprophyres and phonolites of Paresis (Trumbull et al. 2000), are suggested to be uncontaminated or only slightly affected by crustal contamination during the uprising of their melts.

Milner and Le Roex (1996), Le Roex and Lanyon (1998), Harris et al. (1999), and Trumbull et al. (2000) interpret the isotopic compositions of Sr, Nd, and Pb of these rocks to reflect, at least in part, a Tristan plume mantle component. Trumbull et al. (2003) support this model by quantifying the isotopic Sr and Nd variation ranges of the Tristan Plume Mantle at 130 Ma (Fig. 8, "Tristan Plume Box" after Trumbull et al. 2003). For Kalkfeld, a magma formation related to the Tristan Plume clearly is excluded because
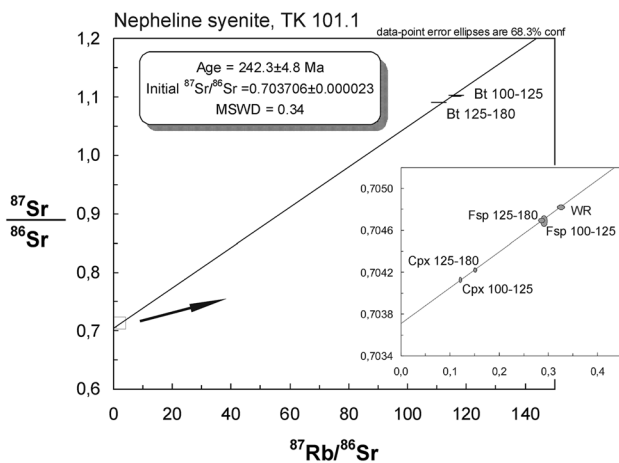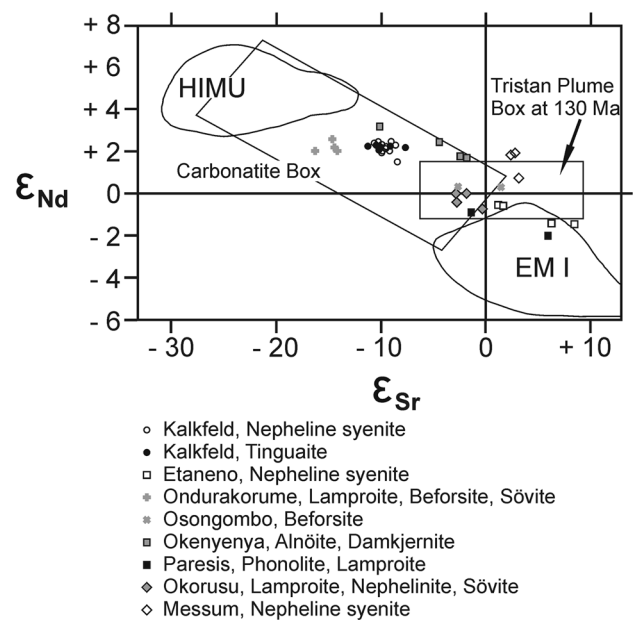
Fig. 6 Rb–Sr isochron diagram for minerals separated from Kalkfeld nepheline syenite TK 101.1 (*Bt* biotite, *Cpx* clinopyroxene, *Fsp* feldspar, *WR* whole rock)
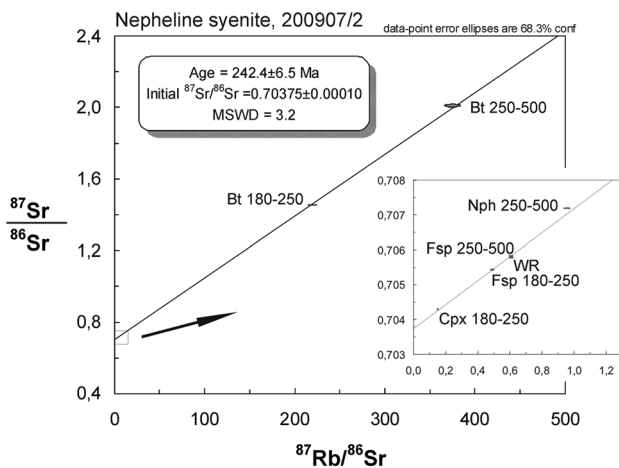
Fig. 7 Rb–Sr isochron diagram for minerals separated from Kalkfeld nepheline syenite 200907/2 (*Bt* biotite, *Cpx* clinopyroxene, *Fsp* feldspar, *Nph* nepheline, *WR* whole rock)

Fig. 8 ε_{Sr}–ε_{Nd} diagram for Kalkfeld nepheline syenite and tinguaite data at 242 Ma. For comparison, the figure also shows the initial isotopic signatures of basic, alkaline, and carbonatite rocks from complexes of the Cretaceous Damaraland Alkaline Province. Carbonatite box defined by Harmer and Gittins (1998). The variation fields of the mantle components HIMU and EM I summarize the data sets for ocean island basalts dominated by these reservoirs (Hofmann 1997). The data for the Tristan Plume Box at 130 Ma are taken from Trumbull et al. (2000)

of the 100 Ma age difference. It follows that the isotopic data of Kalkfeld rocks are not relevant in defining a Tristan Plume mantle composition (cf. Le Roex and Lanyon 1998; Trumbull et al. 2000).

For many carbonatites, the isotopic compositions of Sr, Nd, and Pb show a remarkable similarity to those of ocean island basalts (Bell 1994; Bell and Tilton 2001; Bell and Simonetti 2010). Following interpretations of the magma sources of ocean island basalts (e.g., Zindler and Hart 1986; Hart et al. 1992), contributions from HIMU and EM I mantle reservoirs have also been proposed for carbonatite magma, e.g., for the young carbonatites from the East African rift system (Bell and Tilton 2001). This is expressed in Fig. 8 by the position of the "carbonatite box" (for carbonatites with ages <200 Ma, Harmer and Gittins 1998)

between the HIMU and EM I fields. The basic, alkaline, and carbonatite rocks of the Early Cretaceous Damaraland complexes show a close correspondence to the Tristan OIBs on this diagram, which just reflects a variation of the HIMU–EM I mixing ratios (Fig. 8). This becomes especially plausible when the isotope data of the Damaraland alkaline and carbonatite complexes as reported by Le Roex and Lanyon (1998) and Trumbull et al. (2003) are included into consideration. The isotope data and the temporal association with the Tristan plume fit the picture of a sub-lithospheric melt generation by thermal perturbations within the asthenospheric mantle as outlined in great detail for carbonatites by Bell and Simonetti (2010). However, it does not prove a plume origin, unless the term plume includes every also small-scale thermal perturbation within the Earth's mantle (cf. Bell and Simonetti (2010).

The Middle Triassic emplacement age of the Kalkfeld Complex rules out a magma formation induced by the Tristan Plume. The initial Sr and Nd isotopic signatures of the Kalkfeld samples, however, are similar to the signatures of basic and alkaline samples of the Cretaceous complexes and both the older and the younger magmas are interpreted as mixtures of HIMU and EM I mantle components. The high volumes and short duration of magmatism in the

Paraná-Etendeka province argue for a different geodynamic setting than the singular occurrence of the Kalkfeld Complex. For the latter, small-scale mantle upwellings in the form of "hot fingers" (Wilson and Patterson 2001) within the Damara Zone of lithospheric weakness appears a reasonable scenario.

References

Alberti A, Castorina F, Censi P, Comin-Chiaramonti P, Gomes CB (1999) Geochemical characteristics of Cretaceous carbonatites from Angola. J Afr. Earth Sci 29:735–759

Bailey DK (1992) Episodic alkaline igneous activity across Africa: implications for the causes of continental break-up. In: Storey BC, Alabaster T, Pankhurst RJ (eds) Magmatism and the causes of continental break-up. Geol Soc Spec Pub 68:91–98

Bailey DK (1993) Carbonate magmas. J Geol Soc Lond 150:637–651

Bailey DK, Woolley AR (1999) Episodic rift magmatism: the need for a new paradigm in global dynamics. GeoLines 9:15–20

Bell K (1994) Carbonatites and mantle evolution: a review. Goldschmidt Conference Edinburgh 1994 Abstracts: 69–70

Bell K, Simonetti A (2010) Source of parental melts of carbonatites—critical isotopic constraints. Min Petrol 98:77–89

Bell K, Tilton GR (2001) Nd, Pb and Sr isotope compositions of East African carbonatites: evidence for mantle mixing and plume inhomogeneity. J Petrol 42:1927–1945

Binks RM, Fairhead JD (1992) A plate tectonic setting for Mesozoic rifts of West and Central Africa. In: Ziegler PA (ed) Geodynamics of rifting, vol. II, Case studies on rifts: North and South America and Africa. Tectonophysics 213:141–151

Bühn B (2008) The role of the volatile phase for REE and Y fractionation in low-silica carbonate magmas: implications from natural carbonatites, Namibia. Min Petrol 92:453–470

Bühn B, Rankin AH (1999) Composition of natural, volatile-rich Na–Ca–REE-Sr carbonatitic fluids trapped in fluid inclusions. Geochim Cosmochim Acta 63:3781–3797

Bühn B, Trumbull RB (2003) Comparison of petrogenetic signatures between mantle-derived alkali silicate intrusives with and without associated carbonatite, Namibia. Lithos 66:201–221

Bühn B, Wall F, Le Bas MJ (2001) Rare-earth element systematics of carbonatitic fluorapatites, and their significance for carbonatite magma evolution. Contrib Mineral Petrol 141:572–591

Comin-Chiaramonti P, Marzoli A, Gomes CB, Milan A, Riccomini C, Velásquez VF, Mantovani MMS, Renne P, Tassinari CCG, Vasconcelos PM (2007a) Origin of post-Paleozoic magmatism in Eastern Paraguay. In: Foulger GR, Jurdy DM (eds) Plates, plumes and planetary processes. GSA Spec Paper 430:603–633

Comin-Chiaramonti P, Gomes CB, Cundari A, Castorina F, Censi P (2007b) A review of carbonatitic magmatism in the Paraná-Angola-Namibia (PAN) system. Per Mineralogia 76:25–78

Daly MC, Chorowicz J, Fairhead D (1989) Rift basin evolution in Africa: the influence of reactivated steep basement shear zones. In: Cooper MA, Williams GD (eds) Inversion tectonics. Geol Soc London, Spec Publ 44:309–334

Droop GTR (1987) A general equation for estimating Fe3+ concentrations in ferromagnesian silicates and oxides from microprobe analyses, using stoichiometric criteria. Min Mag 51:431–435

Ferguson AK (1977) The natural occurrence of aegirine—neptunite solid solution. Contrib Mineral Petrol 60:247–253

Gladczenko TP, Hinz K, Eldholm O, Meyer H, Neben S, Skogseid J (1997) South Atlantic volcanic margins. J Geol Soc Lond 154:465–470

Gomes CB, Laurenzi MA, Censi P, DeMin A, Velázquez VF, Comin-Chiaramonti P (1996) Alkaline magmatism from northern Paraguay (Alto Paraguay): a Permotriassic province. In: Comin-Chiaramonti P, Gomes CB (eds) Alkaline magmatism in Central-Eastern Paraguay. Relationships with coeval magmatism in Brazil. Edusp Fapesp, Sao Paulo, Brazil, pp 223–230

Harmer RE, Gittins J (1998) The case for primary, mantle-derived carbonatite magma. J Petrol 39:1895–1903

Harris C (1995) Oxygen isotope geochemistry of the Mesozoic anorogenic complexes of Damaraland, Northwest Namibia: evidence for crustal contamination and its effect on silica saturation. Contrib Mineral Petrol 122:308–321

Harris C, Marsh JS, Milner SC (1999) Petrology of the alkaline core of the Messum igneous complex, Namibia: evidence for the progressively decreasing effect of crustal contamination. J Petrol 40:1377–1397

Hart SR, Hauri EH, Oschmann LA, Whitehead JA (1992) Mantle plumes and entrainment: isotopic evidence. Science 256:517–520

Harry DL, Sawyer DS (1992) Basaltic volcanism, mantle plumes, and the mechanics of rifting: the Parana flood basalt province of South America. Geology 20:207–210

Haschke M (1996) Energy dispersive X-ray spectroscopy for the determination of trace and main elements. J Physique IV Colloque 06:C4-619-C4-625

Hawkesworth CJ, Gallagher K, Kelley S, Mantovani M, Peate DW, Regelous M, Rogers NW (1992) Paraná magmatism and the opening of th South Atlantic. In: Storey BC, Alabaster T, Pankhurst RJ (eds) Magmatism and the causes of continental breakup. Geol Soc London, Spec Publ 68:221–240

Hegenberger W (1988) Karoo sediments of the Erongo Mountains, their environmental setting and correlation. Commun Geol Survey SWAfrica/ Namibia 4:51–57

Hofmann AW (1997) Mantle geochemistry: the message from oceanic volcanism. Nature 385:219–229

Holzförster F, Stollhofen H, Lorenz V, Stanistreet IG (1998) The Waterberg basin in Central Namibia: transfer fault activity during early South Atlantic rift evolution. J Afr Earth Sci 27:116–117

Jerram D, Mountney N, Holzförster F, Stollhofen H (1999) Internal stratigraphic relationships in the Etendeka Group in the Huab Basin, NW Namibia: understanding the onset of flood volcanism. J Geodyn 28:393–418

Jourdan F, Feraud G, Bertrand H, Kampunzu AB, Tshoso G, Watkeys MK, Le Gall B (2005) Karoo large igneous province: brevity, origin, and relation to mass extinction questioned by new $^{40}Ar/^{39}Ar$ age data. Geology 33:745–748

Kinny PD, Compston W, Bristow JD, Williams IS (1989) Archaean mantle xenocrysts in a Permian kimberlite: two generations of kimberlitic zircon in Jwaneng DK2, southern Botswana. Geol Soc Australia, Spec Publ 14:833–842

Körner T (2003) Die Fenit-Aureole des Kalkfeld-Karbonatit-Komplexes, Namibia—Fluid-gebundener Stofftransfer von Alkali- und Spurenelementen. Dissertation, RWTH Aachen University

Körner T, Sindern S, Kramm U (2001) Mineral chemistry in fenites of the Kalkfeld carbonatite complex and its bearing on the composition of the fenitising fluid. J Afr Earth Sci 32:A23

Lambiase JJ (1989) The framework of African rifting during the Phanerozoic. In: Rosendahl B (ed): African rifting. J Afr Earth Sci, Spec Publ 8:183–190

Le Roex AP, Lanyon R (1998) Isotope and trace element geochemistry of Cretaceous Damaraland lamprophyres and carbonatites, northwestern Namibia: Evidence for plume—lithosphere interactions. J Petrol 39:1117–1146

Ludwig KR (2003) Isoplot 3.00. Berkeley Geochronology Center, Spec Publ 4: 70

Lugmair GW, Marti K (1978) Lunar initial ^{143}Nd/^{144}Nd: differential evolution of the lunar crust and mantle. Earth Planet Sci Lett 39:349–357

Marsh JS (1973) Relationships between transform directions and alkaline igneous rock lineaments in Africa and South America. Earth Planet Sci Lett 18:317–323

Martin H, Mathias M, Simpson EWS (1960) The Damaraland subvolcanic ring complexes in South West Africa. 21st Int geol Congr 13:156–174

Miller RMcG (1983) The Pan-African Damara Orogen of South West Africa/ Namibia. In: Miller RMcG (ed) Evolution of the Damara Orogen of South West Africa/ Namibia. Spec Publ Geol Soc South Africa 11:431–515

Miller RMcG (2008) Neoproterozoic and early Palaeozoic rocks of the Damara Orogen. In: Miller RMcG (ed) The geology of Namibia. Geol Surv Namibia 2:13.1–13.410

Miller RMcG (2013) Comparative stratigraphic and geochronological evolution of the Northern Damara Supergroup in Namibia and the Katanga Supergroup in the Lufilian Arc of Central Africa. J Geol Ass Can 40:118–140

Milner SC, Le Roex AP (1996) Isotope characteristics of the Okenyenya igneous complex, northwestern Namibia: constraints on the composition of the early Tristan plume and the origin of the EM I mantle component. Earth Plan Sci Lett 141:277–291

Milner SC, Le Roex AP, O'Connor JM (1995) Age of Mesozoic igneous rocks in northwestern Namibia, and their relationship to continental breakup. J geol Soc Lond 152:97–104

Morimoto N, Fabries J, Ferguson AK, Ginzburg IV, Ross M, Seifert FA, Zussman J, Aoki K, Gottardi G (1988) Nomenclature of pyroxene. Am Mineralogist 73:1123–1133

Müller B (1996) Ring complexes of the Damaraland alkaline province, Namibia, in the light of geochemistry and Rb–Sr, U-Pb, Pb-Pb isotopes. Dissertation, ETH Zürich

Prins P (1981) The geochemical evolution of the alkaline and carbonatite complexes of the Damaraland Igneous Province, South West Africa. Ann University Stellenbosch Serie A1(3):145–278

Renne PR, Ernesto M, Pacca IG, Coe RS, Glen JM, Prevot JM, Perrin M (1992) The age of Paraná flood volcanism, rifting of Gondwanaland, and the Jurassic—Cretaceous boundary. Science 258:975–979

Schmitt AK, Emmermann R, Trumbull RB, Bühn B, Henjes-Kunst F (2000) Petrogenesis and 40Ar/39Ar geochronology of the Brandberg Complex, Namibia: evidence for a major mantle contribution in metaluminous and peralkaline granites. J Petrol 41:1207–1239

Siedner G, Mitchell JG (1976) Mesozoic volcanism in Namibia and Brazil: a K-Ar isochron study bearing on the opening of the South Atlantic. Earth Plan Sci Lett 30:292–302

Sirbescu M, Jenkins DM (1999) Experiments on the stability of cancrinite in the system Na$_2$O–CaO–Al$_2$O$_3$–SiO$_2$–CO$_2$–H$_2$O. Am Mineralogist 84:1850–1860

Steiger RH, Jäger E (1977) Subcommision on geochronology: convention on the use of decay constants in geo- and cosmochronology. Earth Plan Sci Lett 36:358–362

Stephens WE, Calder A (2004) Analysis of non-organic elements in plant foliage using polarized X-ray spectrometry. Anal Chim Acta 527:89–96

Stollhofen H (1999) Karoo Synrift-Sedimentation und ihre tektonische Kontrolle am entstehenden Kontinentalrand Namibias. Z dtsch Geol Ges 149:519–632

Thompson RN, Gibson SA (1991) Subcontinental mantle plumes, hot spots and pre-existing thinspots. J Geol Soc Lond 89:973–977

Thompson RN, Gibson SA, Dickin AP, Smith PM (2001) Early Cretaceous basalt and picrite dykes of the southern Etendeka region, NW Namibia: windows into the role of the Tristan mantle plume in Parana-Etendeka magmatism. J Petrol 42:2049–2081

Trumbull RB, Emmermann R, Bühn B, Gerstenberger H, Mingram B, Schmitt A, Volker F (2000) Insights on the genesis of the Cretaceous Damaraland igneous complexes in Namibia from a Nd- and Sr-isotopic perspective. Commun geol Surv Namibia 12:313–324

Trumbull RB, Bühn B, Romer RL, Volker F (2003) The petrology of basanite—tephrite intrusions in the Erongo complex and implications for the plume origin of Cretaceous alkaline complexes in Namibia. J Petrol 44:93–112

Trumbull RB, Vietor T, Hahne K, Wackerle R, Ledru P (2004) Aeromagnetic mapping and reconnaissance geochemistry of the Early Cretaceous Henties Bay-Outjo dike swarm, Etendeka Igneous Province, Namibia. J Afr Earth Sci 40:17–29

Turner SP, Regelous M, Kelley S, Hawkesworth CJ, Mantovani MSM (1994) Magmatism and continental break-up in the South Atlantic: high precision ^{40}Ar-^{39}Ar geochronology. Earth Plan Sci Lett 121:333–348

Van Zijl PJ (1962) The geology, structure and petrology of the alkaline intrusions of Kalkfeld and Okorusu and the invaded Damara rocks. Ann University Stellenbosch, Serie A37:237–340

Verwoerd WJ (1967) The carbonatites of South Africa and South West Africa. Geological Survey, Handbook 6:452 pp

Verwoerd WJ (1993) Update on carbonatites of South Africa and Namibia. S Afr J Geol 96:75–95

Wanke A, Stollhofen H (2000) The long-lived rift evolution prior break-up of Gondwanaland: evidence from the Karoo-Etendeka depositories in NW-Namibia. J Afr Earth Sci 30:86–87

White R, McKenzie D (1989) Magmatism at rift zones: the generation of volcanic continental margins and flood basalts. J Geophys Res 94:7685–7729

Whitney DL, Evans BW (2010) Abbreviations for names of rock-forming minerals. Am Mineralogist 95:185–187

Wigand M, Schmitt AK, Trumbull RB, Villa IM, Emmermann R (2004) Short-lived magmatic activity in an anorogenic subvolcanic complex: 40Ar/39Ar and ion microprobe U–Pb zircon dating of the Erongo, Damaraland, Namibia. J Volcan Geotherm Res 130:285–305

Wilson M, Patterson R (2001) Intraplate magmatism related to short-wavelength convective instablilities in the upper mantle: evidence from the Tertiary-Quarternary volcanic province of western and central Europe. In: Ernst RE, Buchan KL (eds) Mantle plumes: their identification through time. Geol Soc Am, Spec Paper 352:37–58

Woolley AR, Platt RG, Eby GN (1996) Relatively aluminous alkali pyroxene in nepheline syenites from Malawi: mineralogical response to metamorphism in alkaline rocks. Can Mineralogist 34:423–434

Ziegler URF (1992) Preliminary results of geochemistry, Sm–Nd and Rb–Sr studies of post-Karoo carbonatite complexes in Southern Africa. Schweiz Mineral Petrogr Mitteilungen 72:135–142

Zindler A, Hart S (1986) Chemical geodynamics. Ann Rev Earth Planet Sci 14:493–571